Application of MEMS Data to Fast Inversion of Rupture Process: Tests with Recordings from the IRREEW Network

Chenyu Xu[1], Yong Zhang[*,1], Rongjiang Wang[2], Sibo Hua[1], Yueyi Xu[3], Danqing Dai[4], Yao Pang[5], and Jinrong Su[5]

Abstract

The China Earthquake Administration established a network for intensity rapid report and earthquake early warning (IRREEW) in 2016–2020, which consists of approximately 5000 conventional strong-motion and approximately 10,000 low-cost micro-electro-mechanical system (MEMS) seismometers. These seismographs, particularly MEMS stations, can provide a large amount of near-field waveform data suitable for rapid source inversion. Compared with conventional strong-motion data, MEMS recordings have rarely been used in the previous source inversions, because the MEMS technology is newly applied in earthquake monitoring, and the seismograph has a relatively lower signal-to-noise ratio and more severe baseline shifts. However, from waveform comparisons at collocated MEMS and strong-motion stations, we find that they are highly consistent with each other, particularly at frequencies above 0.04 Hz. To explore the application prospect of MEMS data to source inversion, we inverted both MEMS and strong-motion data for three strong earthquakes recorded by the IRREEW network during 2021–2022 to determine their rupture processes. In applications to the 2021 M_w 6.1 Yangbi earthquake, the 2022 M_w 6.6 Menyuan earthquake, and the 2022 M_w 6.6 Luding earthquake, the MEMS data equally well constrain the rupture model. The resulting source information, including the moment magnitude, rupture direction, and rupture dimension, are consistent with those obtained from the strong-motion inversions. Because the low-cost MEMS instruments can be deployed densely around seismically active regions, they can provide urgent waveform data for rapid determination of rupture process, which is crucial for simulation of strong ground motions, and assessments of earthquake and related disasters.

Introduction

Fast determination of earthquake source parameters plays an increasingly important role in postearthquake responses (Kanamori *et al.*, 1997; Yue *et al.*, 2020). Various works, including event identification, event location and magnitude measurement, moment tensor inversion, estimation of intensity distribution, and rupture process inversion based on different models from a point source to a finite fault can provide urgent information for emergency response and early warning (Kanamori and Rivera, 2008; Ekström *et al.*, 2012; Zhang *et al.*, 2012, 2014; Kuang *et al.*, 2021). Among these works, the source rupture process contains the most detailed information for obtaining a complete picture of an earthquake. Once the rupture model of an earthquake is obtained, we can simulate the strong ground motions to better estimate the casualties and economic losses, and assess the risks posed by secondary disasters such as landslides.

Rapid inversion of rupture process can be performed with teleseismic, regional, and near-field waveform data, among which the near-field data are recorded the earliest and can better constrain the rupture behavior (Zhang *et al.*, 2012). At present, high-rate Global Positioning System (GPS) and strong-motion data are two major near-field waveform recordings that can be observed close to the source or fault (Yue and Lay, 2011; Zhang *et al.*, 2014). However, because of their relatively high-cost, high-rate GPS and strong-motion stations are still sparse in many areas, greatly limiting the efficiency

1. School of Earth and Space Science, Peking University, Beijing, China; 2. Helmholtz Centre Potsdam, GFZ German Research Centre for Geosciences, Potsdam, Germany; 3. Institute of Earthquake Forecasting, China Earthquake Administration, Beijing, China; 4. China Earthquake Networks Center, Beijing, China; 5. Sichuan Earthquake Administration, Chengdu, China

*Corresponding author: zhang-yong@pku.edu.cn
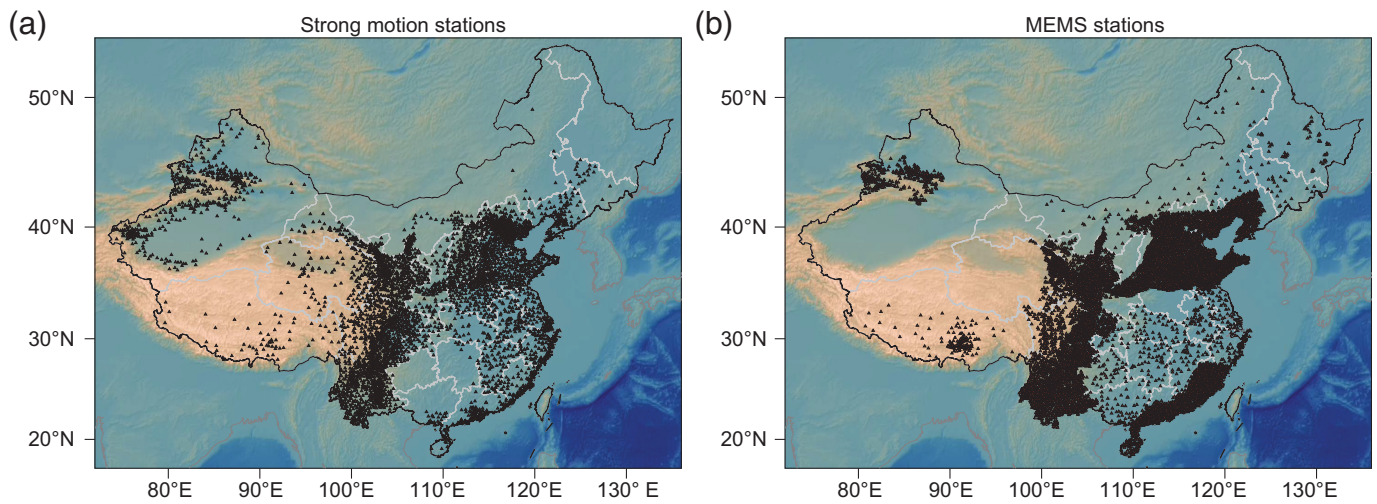
© Seismological Society of America

Figure 1. Locations of the (a) strong-motion and (b) micro-electro-mechanical system (MEMS) stations in the intensity rapid report and earthquake early warning network.

and capability of earthquake responses. The micro-electromechanical system (MEMS) is a low-cost accelerometer that can record near-fault ground motions (Eddy and Sparks, 1998; Lin, 2011). Benefiting from the low cost, the MEMS can be used to establish a dense network economically. At present, MEMS seismometers have been deployed and operated by many institutes and universities (D'Alessandro et al., 2019), including the Japan Meteorological Agency (Horiuchi et al., 2009), Stanford University (Cochran, Lawrence, Christensen, and Chung, 2009; Cochran, Lawrence, Christensen, and Jakka, 2009), Italy Ministry of Education, Universities and Research (D'Alessandro et al., 2018), and National Taiwan University (Wu et al., 2013; Wu, 2015), in many countries and regions to improve the earthquake monitoring ability.

The China Earthquake Administration established a network for intensity rapid report and earthquake early warning (IRREEW) in 2016–2020, which consists of approximately 5000 conventional strong-motion and approximately 10,000 MEMS accelerographs (Peng et al., 2019; Li et al., 2021; Fig. 1). The interstation spacing of the large-scale IRREEW network reaches 10–20 km in many seismically active areas, providing a large number of near-field waveform recordings. Many previous studies have confirmed that the P-wave initial motion, amplitude, shaking duration or waveform length, and waveform shape of the MEMS data are consistent with those of the conventional strong-motion data (Holland, 2003; Aizawa et al., 2008; Lin, 2011; Pozzi et al., 2011; Lawrence et al., 2014; Saunders et al., 2016; Bravo-Haro et al., 2021; Peng et al., 2021). Thus, they can be used for earthquake location, magnitude measurement, mechanism determination, and intensity estimation. However, MEMS data have rarely been used in source waveform inversions compared with conventional strong-motion records, which have been proven to be effective and reliable (Yokota et al., 2011; Zheng et al., 2017, 2018, 2020). For the IRREEW network, a large proportion of the MEMS seismometers are deployed on soft soil near the mobile
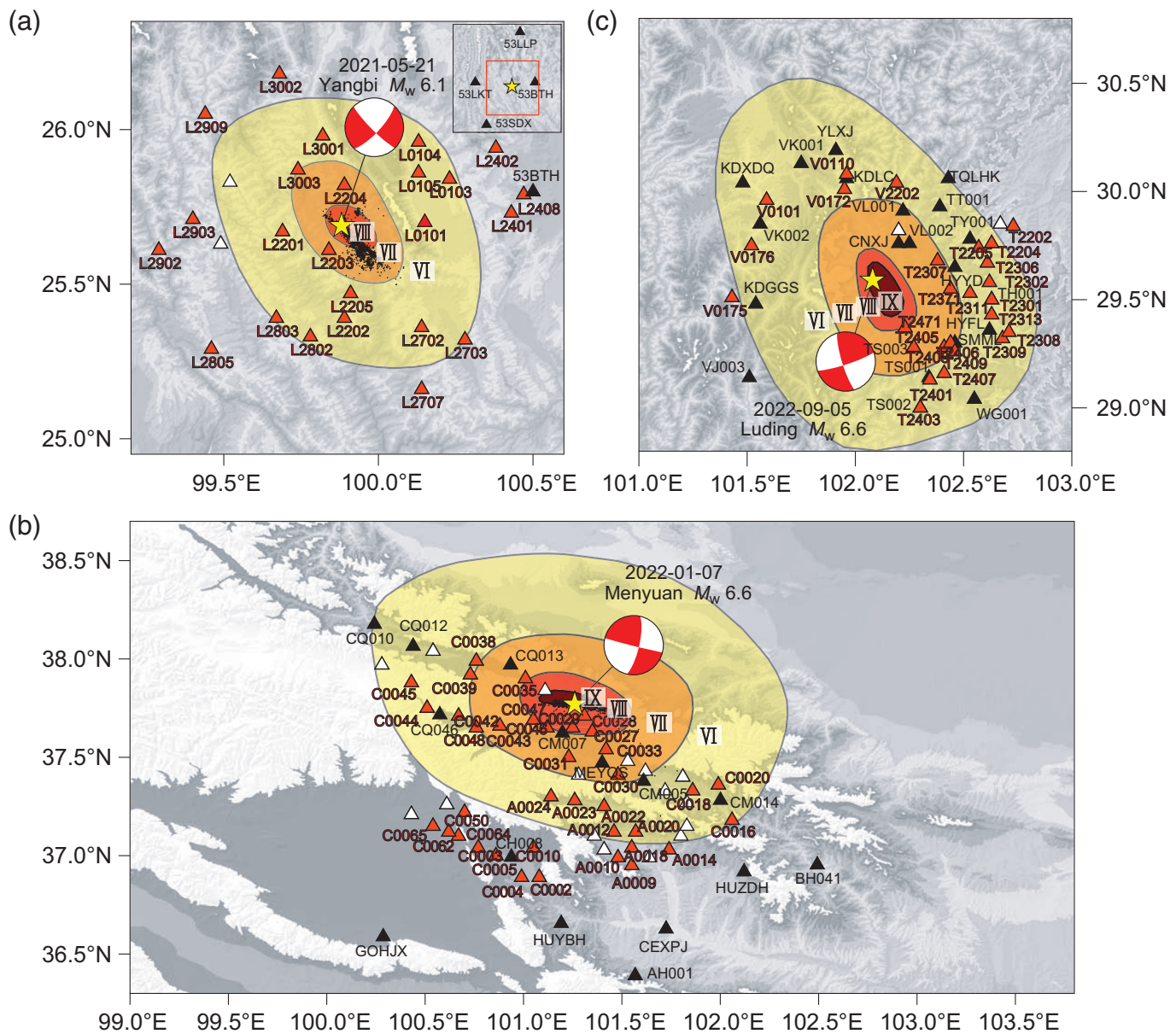
communication towers (Peng et al., 2022), leading to relatively low signal-to-noise ratio (SNR) and more severe baseline shifts. Because MEMS stations constitute the majority of the IRREEW network, it is necessary to conduct inversion tests to examine the applicability of their waveform data in fast source inversions.

Since its completion, the IRREEW network has recorded three significant strong earthquakes with $M_w > 6.0$, that is, the 2021 M_w 6.1 Yangbi earthquake, the 2022 M_w 6.6 Menyuan earthquake, and the 2022 M_w 6.6 Luding earthquake (Fig. 2). In this study, we inverted both the MEMS and strong-motion data for these three earthquakes to obtain finite-fault rupture models. We focused on the performance of the MEMS inversions by comparing their results with those of the strong-motion inversions. If the obtained MEMS models can be demonstrated to be comparable with the strong-motion models, they would play more positive roles in future earthquake monitoring and emergency responses.

Data and Methods
MEMS waveforms and their processing

We obtained the MEMS and strong-motion data for the three strong earthquakes from the China Earthquake Network Center (CENC). Figure 2 shows the MEMS and strong-motion stations used in this study. According to Peng et al. (2022), the MEMS stations of the IRREEW network measure an acceleration range of −19.6 to 19.6 m/s^2 for horizontal components and −19.6 to 19.6 m/s^2 or −29.4 to 9.8 m/s^2 for vertical components. The lower and higher cutoff frequencies are <0.01 and >40 Hz, respectively, which effectively encompass the frequency band of the source waveform inversions. The sensitivity is 500 V/Gal, and the sampling rate is 100 Hz.

Figure 2. Epicentral areas of the (a) 2021 Yangbi, (b) 2022 Manyuan, and (c) 2022 Luding earthquakes. The yellow stars represent the epicenters. The white triangles denote the MEMS stations, and the red triangles are the remaining MEMS stations that were finally used in inversions. The black triangles denote the strong-motion stations. The yellow, orange, and red areas represent the different intensity regions. The black dots denote the locations of the aftershocks.

There are three pairs of collocated MEMS and strong-motion stations for the 2022 Luding earthquake. This presents an opportunity to assess the quality of the MEMS data by comparing them with the strong-motion data at these collocated stations. For comparison, we minimized the effects of the base-line shifts by removing the second-order Legendre polynomial fittings from the raw acceleration records. This operation was also conducted for the integrated velocities. In addition to the unfiltered recordings, all of the waveforms were also compared in the frequency band of concern (0.04–0.5 Hz). As shown in Figure 3 and Figures S1 and S2, available in the supplemental material to this article, most of the acceleration, velocity, and displacement waves of the collocated MEMS and strong-motion station data exhibit similar features. When the frequency is <0.04 Hz, the amplitudes of the MEMS data are larger than those of the strong-motion data, suggesting that they are more noised at low frequencies. However, for frequencies of >0.04 Hz, they are highly consistent with each other, indicating that the MEMS waveforms are of high quality if a high-pass filter with a frequency of 0.04 Hz is applied.

We used the automatic inversion system developed by Zheng *et al.* (2020) based on the iterative deconvolution stacking (IDS) method (Zhang *et al.*, 2014) to invert the MEMS and strong-motion data. Compared with conventional methods in which smoothing weights are usually specified through trial
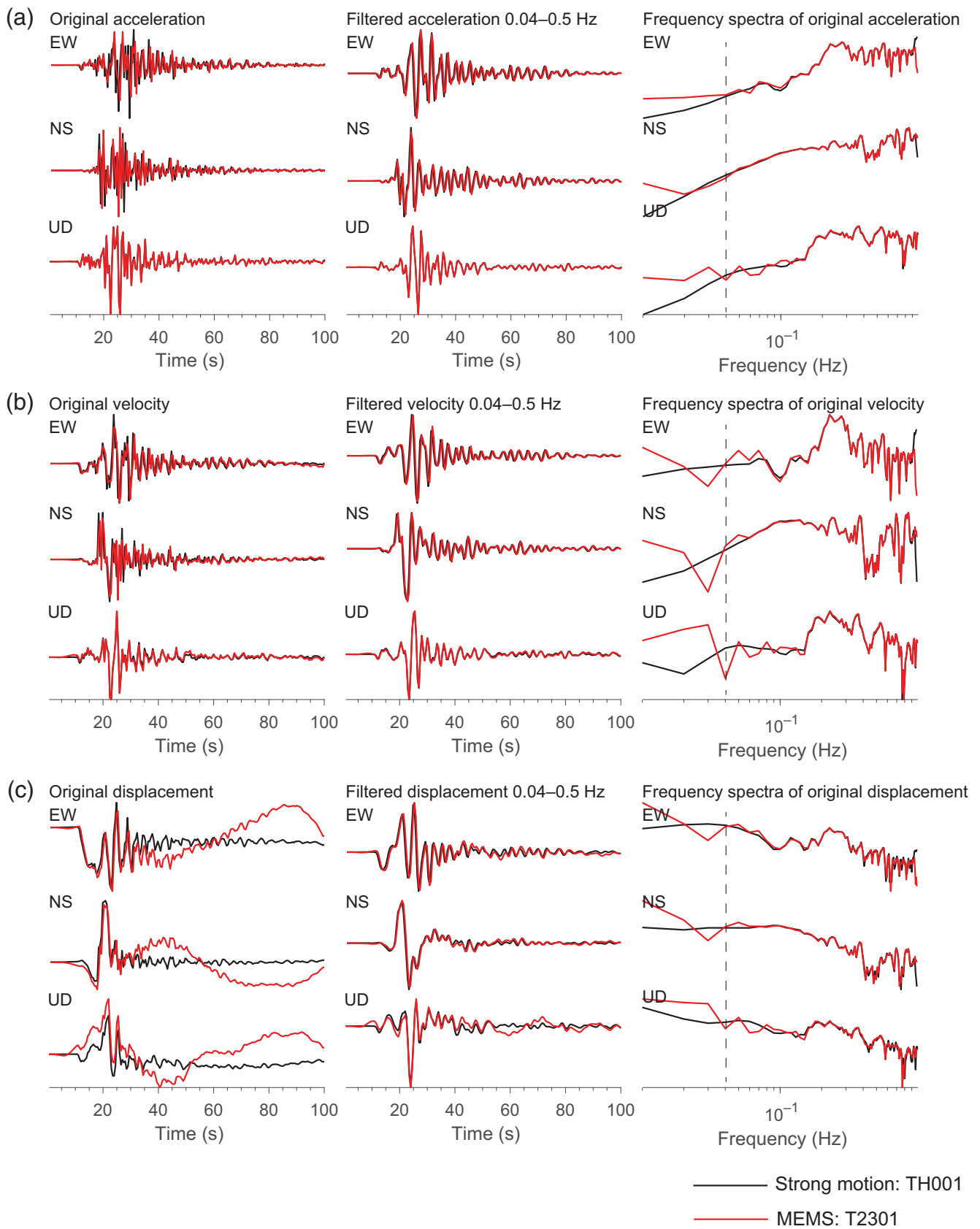
Figure 3. Comparisons of waveforms and spectra for the collocated MEMS (T2301) and strong-motion (TH001) stations for the 2022 Luding earthquake. The black and red lines represent the MEMS and strong-motion waveforms, respectively. Panels (a), (b), and (c) show the waveforms and spectra of the acceleration, velocity, and displacement, respectively. The black dash lines in the right panels denote the frequency of 0.04 Hz.

and error, the automatic IDS inversion system helps to minimize these subjective factors. The origin time and hypocentral location of the Yangbi earthquake were acquired from Yang et al. (2021), those of the Menyuan earthquake were from the U.S. Geological Survey (USGS), and those of the Luding earthquake were obtained from the CENC. To construct the fault model, we adopted the focal mechanisms released by the USGS for the Yangbi and Menyuan earthquakes and Global Centroid Moment Tensor (Global CMT) for the Luding earthquake. The Green's functions were calculated using the QSSP program (Wang et al., 2017) based on the 1D velocity models retrieved from the CRUST1.0 model (Laske et al., 2012).

Waveform screening

Station screening is essential when performing inversions using low-quality data. Zheng et al. (2020) proposed a screening procedure for selecting waveform stations. Initially, this procedure uses an estimated fault size determined from the empirical relationship with the preliminary reported magnitude (Wells and Coppersmith, 1994) to perform the inversion. The fault can be expanded if slips appear at the fault edges. In the station screening, the stations with an average misfit (normalized) of less than 0.6 are retained. To preserve more waveform data, we modified the misfit threshold to 0.8 and removed the stations with poor waveform fittings. Then, a smaller misfit threshold of 0.7 was used to screen each waveform component.

Postprocessing

Because many MEMS stations are deployed on soft soil, they may exhibit strong coda waves, which can lead to an excessively long duration. To address this problem, wherein the source time functions (STFs) contain multiple peaks, we calculated the synthetics and corresponding residuals by cutting the STF at each local minimum. The length of the STF was determined at the inflection point of the residual curve (Fig. 4).

Results

The 2021 M_w 6.1 Yangbi earthquake

The M_w 6.1 Yangbi earthquake occurred in Yunnan Province, southwestern China, at 13:48:34 on 21 May 2021 (UTC). Based on the tectonic setting and aftershock relocation results (Yang et al., 2021), this earthquake ruptured a northwest–southeast-trending fault. The hypocenter was located at 99.88° E, 25.69° N, and a depth of 6 km. The strike, dip, and rake given by the USGS are 135°, 82°, and −165°, respectively. The MEMS rupture model of this earthquake is shown in Figure 4, including the slip distribution, STF, and spatial–temporal rupture process. The synthetic waveforms generated by the rupture model are compared with the observed ones in Figure 5.

As shown in Figure 4a,b, the rupture propagates horizontally toward the southeast and slightly upward. The major rupture area is 1–9 km to the southeast of the hypocenter and is
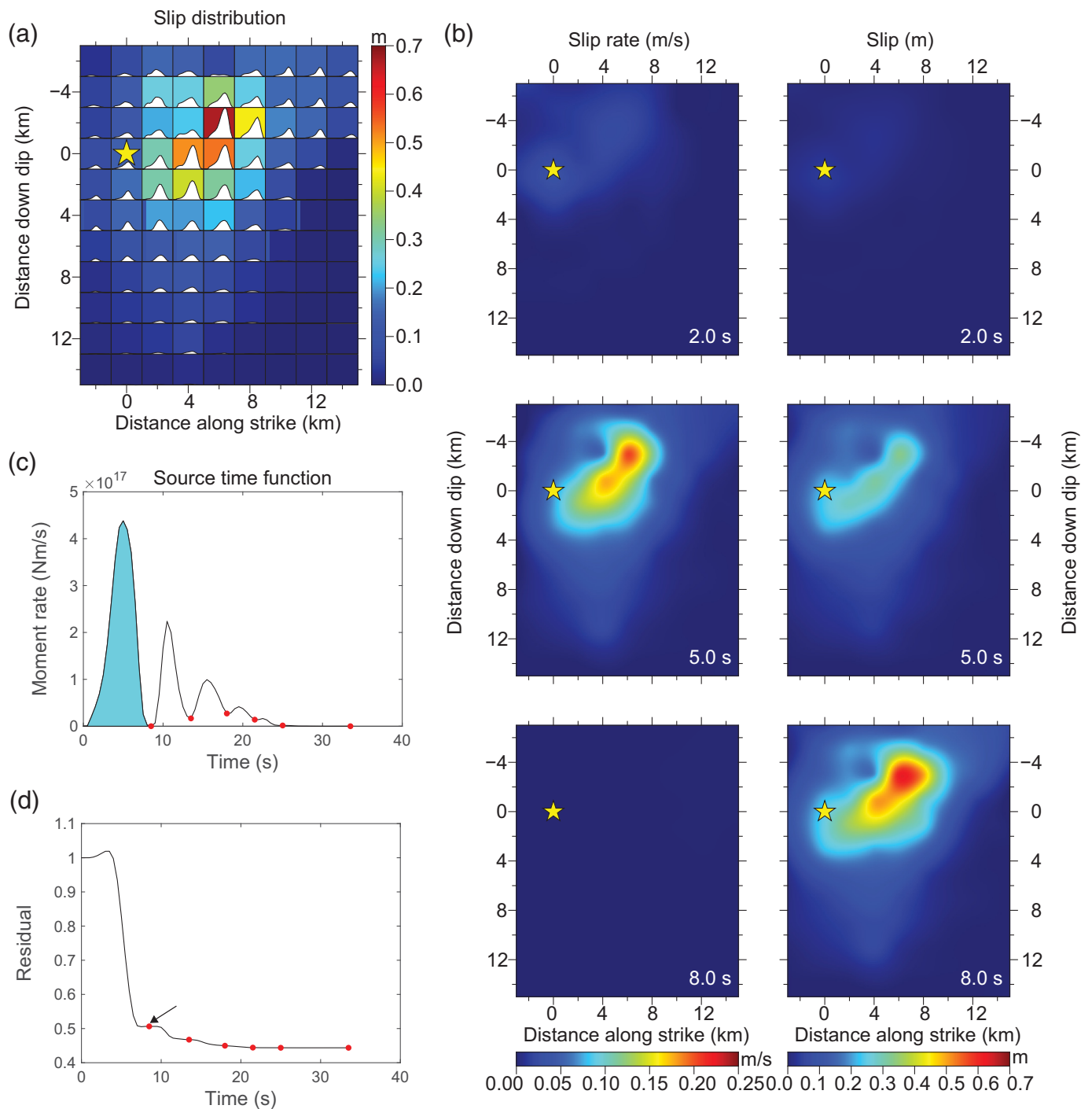
2–10 km deep. The maximum slip is about 0.62 m, and the seismic moment is 1.55×10^{18} N · m, which is equivalent to M_w 6.06. The moment centroid is found to be located 5.20 km away from the hypocenter, and the average rupture velocity is calculated to be 1.09 km/s. Figure 4c,d shows the postprocessing for obtaining an STF with an acceptably small misfit and duration. To improve the computation efficiency, only six STFs were taken into account, starting from 0 s and ending at the time of the six local minima. Then, the normalized misfits between the synthetic and observed waveforms were computed (shown in Fig. 4d). After the first local minimum of 8 s, the seismic moment makes very little contribution to waveform fitting, and the corresponding slips mainly distributed in deep areas where the near-field station have relatively poor resolution (Fig. S3). Therefore, we chose the final STF terminating at the first local minimum (shown in cyan in Fig. 4c).

The Yangbi earthquake was investigated by inverting geodetic Interferometric Synthetic Aperture Radar (InSAR) data (Zhang et al., 2021; Li, Böse, et al., 2022; Lu et al., 2022). These InSAR models show that the main slip area was located at depths of 3–13 (Zhang et al., 2021), 1–14 (Li, Böse, et al., 2022), and 2–11 km (Lu et al., 2022). The maximum slips indicated by these models are 0.61 m at a depth of 6.98 km, 0.6 m at a depth of 5 km, and 1.1 m at a depth of 6 km. The major slip areas are similar to those indicated by our MEMS slip model, but the maximum slips are significantly greater. This difference may be because InSAR inversions commonly choose a smaller subfault size (1 × 1 km) and tend to apply smaller smoothing weights to the inversions.

The 2022 M_w 6.6 Menyuan earthquake

The 2022 M_w 6.6 Menyuan earthquake occurred in the northeast margin of the Qinghai–Tibet plateau, at 17:45:30 on 7 January 2022 (UTC). Because of the poorly accessible conditions of the northern side, the near-field network stations are all located to the south of the epicenter, providing an azimuthal coverage of approximately 180°. Based on the tectonic background and aftershock relocation results (Yang et al., 2022), this earthquake ruptured an east–west-trending fault. The hypocenter was located at 101.26° E, 37.77° N, and a depth of 13 km. The strike, dip, and rake given by the USGS are 104°, 88°, and 15°, respectively. The rupture model inverted from the MEMS data is shown in Figure 6, and the observed and synthetic MEMS waveforms are compared in Figure 7.
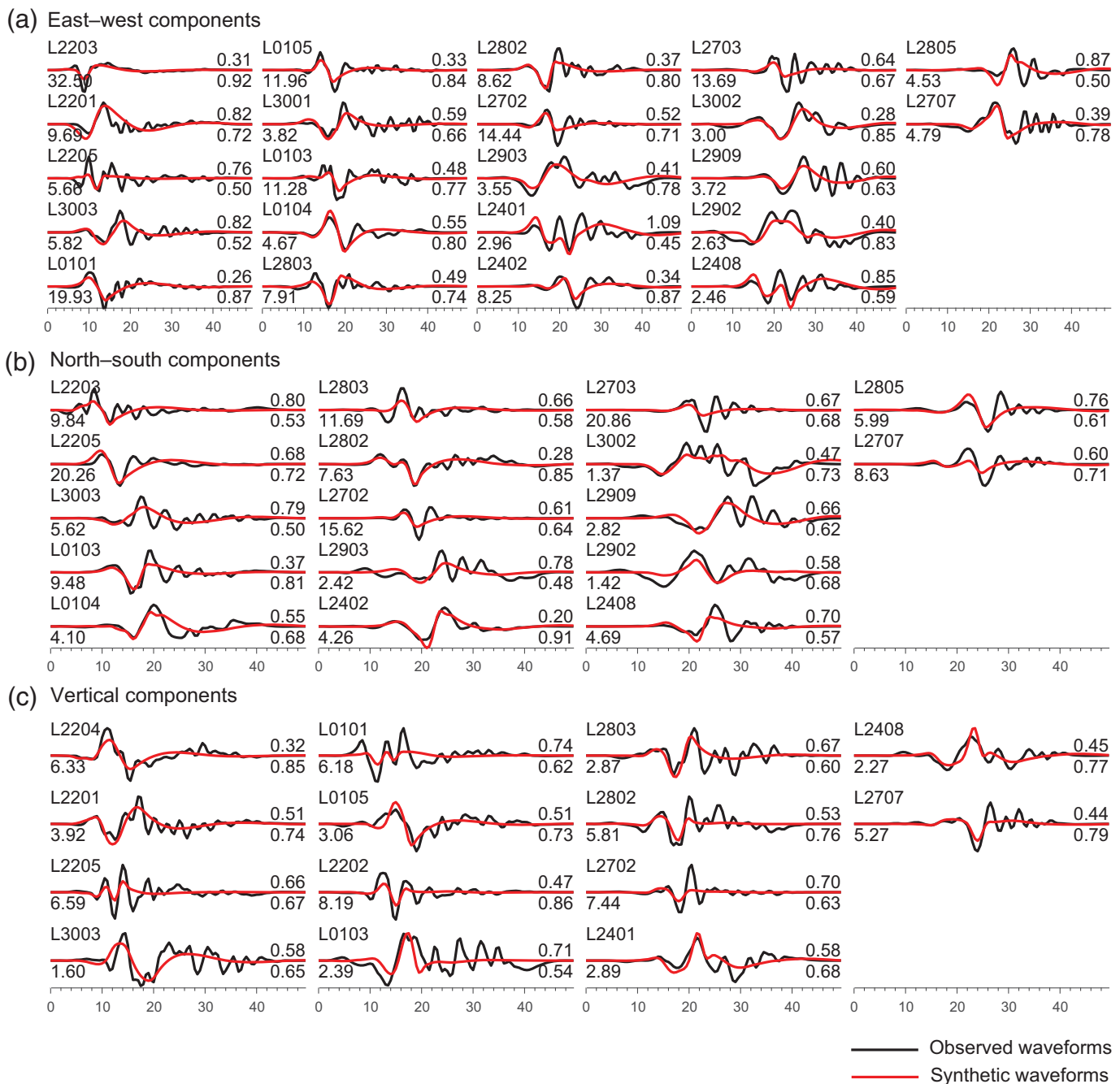
As shown in Figure 6, the rupture mainly propagates upward, with the major rupture area situated above the hypocenter at depths of 0–8 km along a horizontal length of 8 km. The maximum slip is 2.86 m, and the seismic moment is 6.65×10^{18} N · m, which is equivalent to M_w 6.48. The moment centroid is located at −9.04 and −0.88 km in the down-dip and strike directions, respectively. The distance between the centroid and the hypocenter is 9.08 km, and

Figure 4. MEMS rupture model of the Yangbi earthquake. (a) The slip distribution and subfault source time functions (STFs). The yellow stars represent the hypocenter. (b) Snapshots of the rupture process. The left and right columns show the slip rate and slip distributions at different time, respectively. (c) The STF. The red dots represent the local minima. The cyan area denotes the finally chosen STF. (d) The residual curve computed using STFs with different lengths. The arrow denotes the corner point.
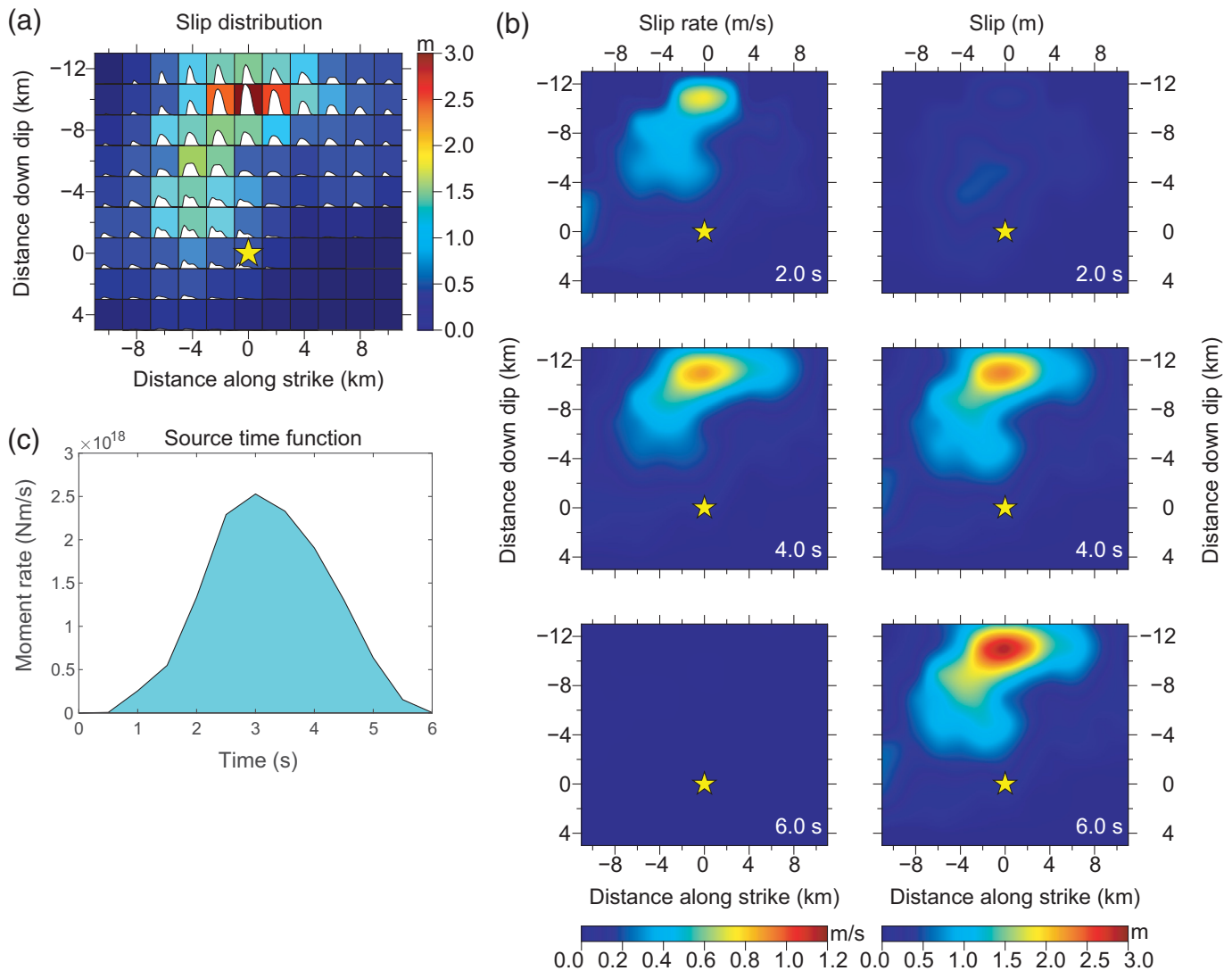
the average rupture velocity is 2.82 km/s. The STF shown in Figure 6c indicates that the duration of the source is approximately 6 s, with the peak moment rate appearing at 3 s.

In existing slip models of the Menyuan earthquake, the major slip area is situated at depths of 0–10 (Yang *et al.,* 2022), 0–8 (Li, Huang, *et al.,* 2022), and 3–9 km (Bao *et al.,* 2022). In addition, the maximum slips are 3.5 m at a depth of 6 km, 3.5 m at a depth of 4 km, and 3.45 m at a depth of 5 km. These models agree with our model regarding the location of the major slip area, but the maximum slips are slightly larger.

Figure 5. (a) East–west, (b) north–south, and (c) vertical components. Three-component waveform fitting for the Yangbi earthquake. The black and red lines represent the observed and synthetic waves, respectively. The maximum amplitude, normalized misfit, and correlation coefficient of each component are observed in the bottom-left, top-right, and bottom-right corners, respectively. The normalized misfit of all of the components is 0.51.

The 2022 Luding earthquake

The 2022 M_w 6.6 Luding earthquake occurred in Sichuan Province, China, at 04:52:18 on 5 September 2022 (UTC). The hypocenter was located at 102.08° E, 29.59° N, and a depth of 10 km. The strike, dip, and rake given by the Global CMT are 163°, 80°, and 8°, respectively. The rupture model determined from the MEMS data inversion is shown in Figure 8, and the corresponding waveform fittings are shown in Figure 9.

The rupture of the earthquake mainly propagates toward the south and upward, and the major rupture area is located 2–14 km to the southeast of the hypocenter at depths of 0–10 km (Fig. 8). The maximum slip is 1.81 m, and the seismic moment is estimated to be 9.50×10^{18} N · m, which is equivalent to M_w 6.58. The moment centroid is situated at −5.86 and 5.88 km in the down-dip and strike directions, respectively, corresponding to a moment centroid 8.30 km away from

Figure 6. MEMS rupture model of the Menyuan earthquake. (a) The slip distribution and subfault STFs. The yellow stars denote the hypocenter. (b) Snapshots of the rupture process. (c) The STF.

the hypocenter. The average rupture velocity is calculated to be approximately 1.64 km/s. The rupture lasts for approximately 12 s, with two moment-rate peaks at 3.5 and 7 s (Fig. 6c).
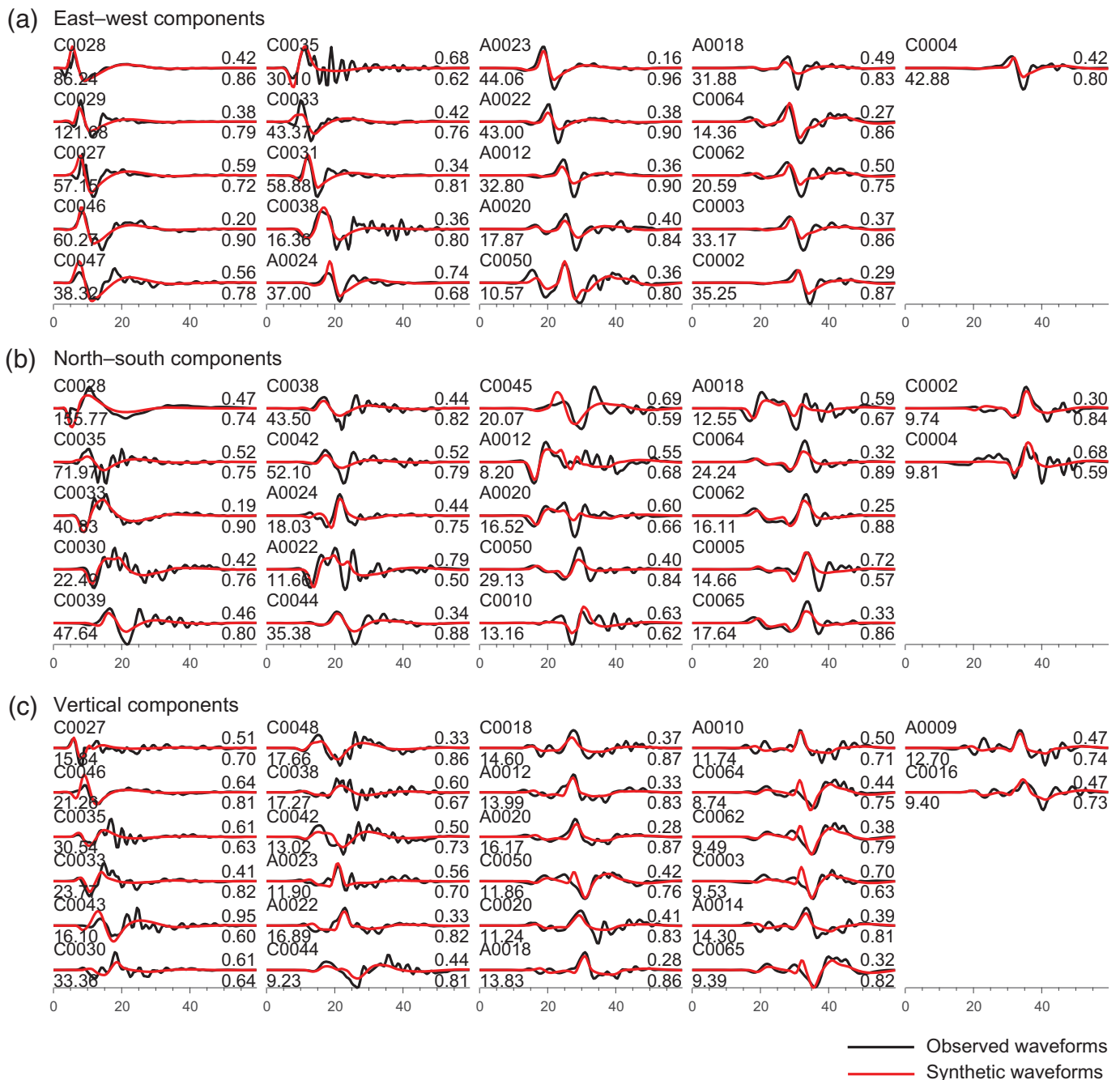
Discussion
Comparison of the MEMS and strong-motion models

The strong-motion data from the IRREEW network commonly have better instrument responses and higher SNRs than the MEMS records due to the design criterion and the site conditions. To examine the reliability of the rupture models obtained from the MEMS data inversions, we also inverted the strong-motion data for the three earthquakes and compared the strong-motion models to the MEMS ones. Because the baseline shifts of the strong-motion data at low frequencies are not so serious, the lower bounds of the frequency band were set to 0.02 Hz. The strong-motion waves in this relatively broad frequency band are well fitted (Figs. S4–S6). For the 2021 Yangbi earthquake, because there are only four faraway strong-motion stations (Fig. 2a), the fault

size was given manually, instead of being determined automatically.

The MEMS and strong-motion models are compared in Figure 10. Both the MEMS and strong-motion models of the 2021 Yangbi earthquake suggest a similar rupture direction: The ruptures mainly propagated toward the southeast and upward (Fig. 10a–c). However, the MEMS model revealed a more concentrated slip area near the hypocenter and a larger peak slip (Fig. 10a). This could be ascribed to the sparseness and further distances of the strong-motion stations (Fig. 2a). The duration of the STFs is also different: The peak moment rate occurs approximately 2 s earlier in the MEMS model than in the strong-motion model. The delayed STF of the strong-motion model could be attributed to the lack of strong-motion stations in the rupture direction (east-southeast). Because of

Figure 7. (a) East–west, (b) north–south, and (c) vertical components. Three-component waveform fitting results for the Menyuan earthquake. The black and red lines represent the observed and synthetic waveforms, respectively. The normalized misfit of all of the components is 0.43.
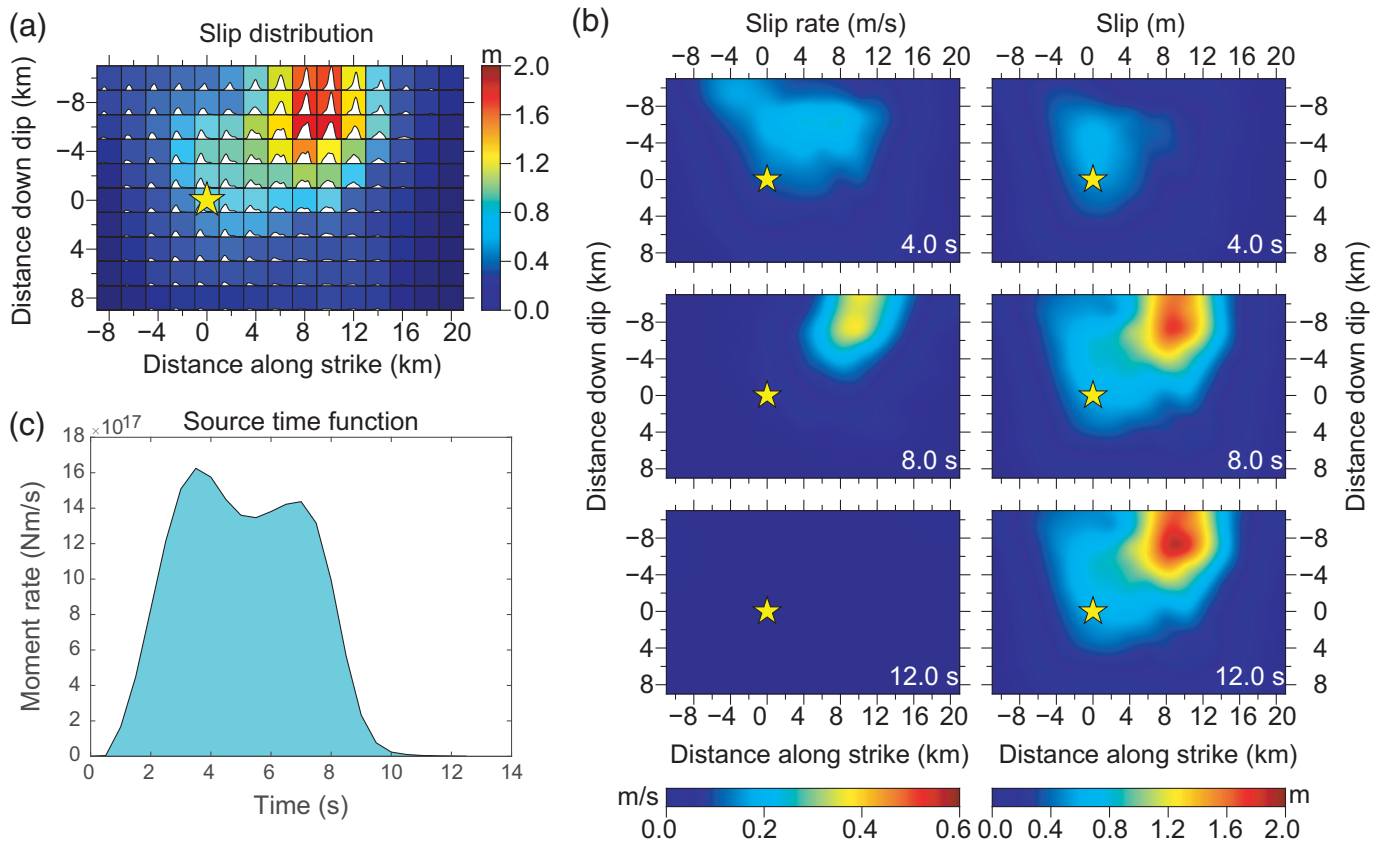
the better coverage of the MEMS network, the slip distribution and the maximum slip of the MEMS model are closer to existing geodetic models (Zhang *et al.*, 2021; Li, Böse, *et al.*, 2022; Lu *et al.*, 2022) in terms of the slip distribution and rupture length, and, thus, they are preferable in this work.

In contrast to the 2021 Yangbi earthquake, the MEMS and strong-motion stations for the 2022 Menyuan earthquake have almost identical coverage in azimuth and takeoff angles (Fig. 10d–f). Accordingly, the two rupture models are close to each other. The maximum slips of the strong-motion model are slightly larger than those of the MEMS model (Table 1), but they are still within an acceptable range.

For the 2022 Luding earthquake, both the MEMS and strong-motion data have an ideal distribution with azimuthal gaps less than 90°. As such, most of the source parameters, including the moment magnitude, peak slip values, slip distributions, STFs, and rupture lengths of the two models are almost identical (Fig. 10g–i). A greater difference is found

Figure 8. Rupture model of the Luding earthquake obtained by inverting the MEMS data. (a) The slip distribution and subfault STFs. The yellow stars represent the hypocenter. (b) Snapshots of the rupture process. (c) The STF.
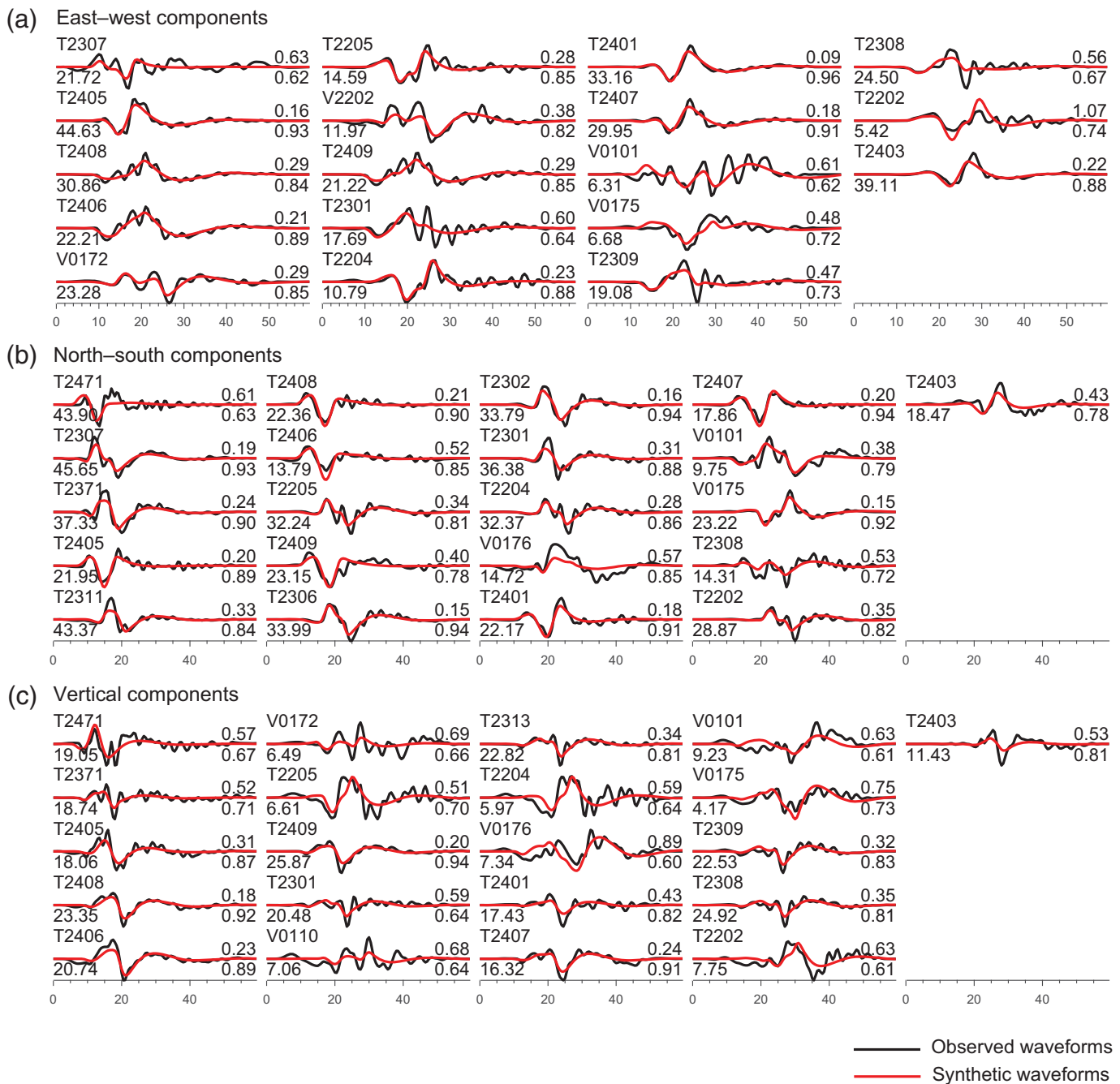
for the average rupture velocities that are sensitive to both spatial and temporal centroids (Table 1).

To compare the MEMS and strong-motion models more quantitatively, we simulated strong-motion synthetics for the MEMS models and the MEMS synthetics for the strong-motion models. Consequently, the normalized misfits for both the networks as well as their combinations could be calculated (Table S1). For the Menyuan and Luding earthquakes, the misfits of the MEMS models are slightly lower than those of the strong-motion models, suggesting that the MEMS data even have a better performance than the strong-motion data.

This indicates that the data quantity can make up for the quality defect to some extent. Nonetheless, for the Yangbi earthquake, the MEMS model could not explain the strong-motion data and vice versa, which is mainly caused by the significant differences in the two networks.

TABLE 1

Comparisons of Several Major Source Parameters from the Micro-Electro-Mechanical System (MEMS) and Strong-Motion Models of the Three Earthquakes

Earthquakes	Rupture Models	M_w	D_{max} (m)	L_c (km)	V_a (km/s)
Yangbi	MEMS	6.06	0.62	5.20	1.09
	Strong motion	6.02	0.37	10.58	1.52
Menyuan	MEMS	6.48	2.86	9.04	2.82
	Strong motion	6.55	3.63	10.13	2.90
Luding	MEMS	6.58	1.81	8.30	1.64
	Strong motion	6.56	1.93	7.31	1.30

D_{max}, maximum slip; L_c, distance between the moment centroid and hypocenter; M_w, moment magnitude; and V_a, average rupture velocity.

Figure 9. (a) East–west, (b) north–south, and (c) vertical components. Three-component waveform fitting results for the Luding earthquake. The black and red lines represent the observed and synthetic waveforms, respectively. The normalized misfit of all of the components is 0.29.
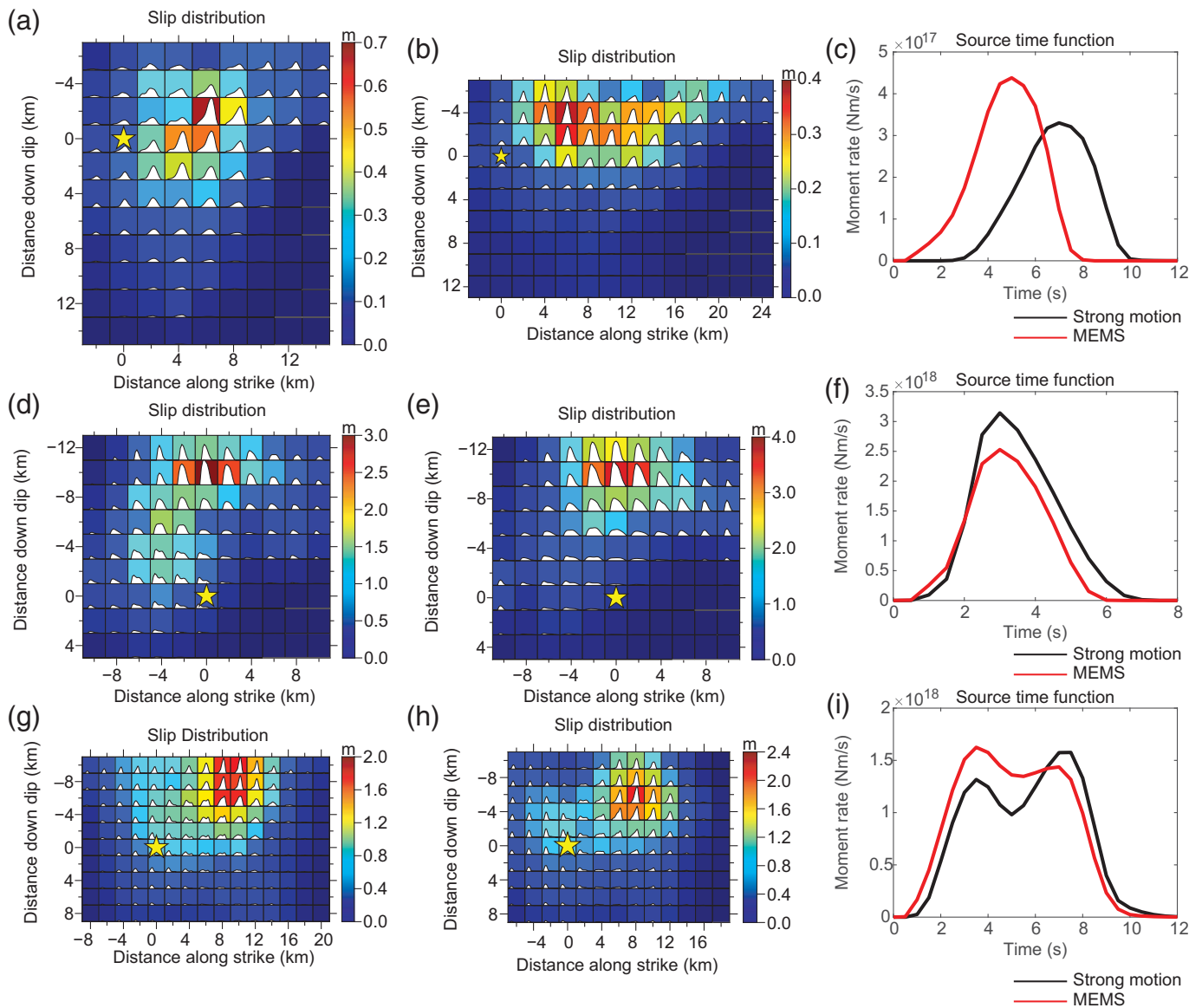
MEMS inversion with different frequency bands

It is necessary to select an appropriate frequency band for finite-fault inversion. Zheng et al. (2020) proposed a criterion for choosing proper frequency bands based on the preliminary magnitude: 0.02–0.5 Hz for $M_w < 6.5$, 0.02–0.2 Hz for M_w 6.5–7.5, 0.02–0.1 Hz for M_w 7.5–8.5, and 0.02–0.05 Hz for $M_w > 8.5$. The upper bounds of the frequency bands are related to the subfault size (Zheng et al., 2020), which is determined by balancing the required resolution and computing time. The lower cutoff frequencies are the main issue we focused on here, because the MEMS records are more noised at low frequencies by baseline shifts (Fig. 3 and Figs. S1 and S2).

Taking the 2022 Menyuan earthquake as an example, we obtained rupture models by inverting the MEMS data with different lower frequency bounds and a fixed upper frequency bound of 0.5 Hz (Fig. 11). The results of the four inversions exhibit similar rupture directions and slip distributions (Fig. 11), but slightly varied maximum slips. In addition, as the lower frequency bound increases, the low-frequency noises
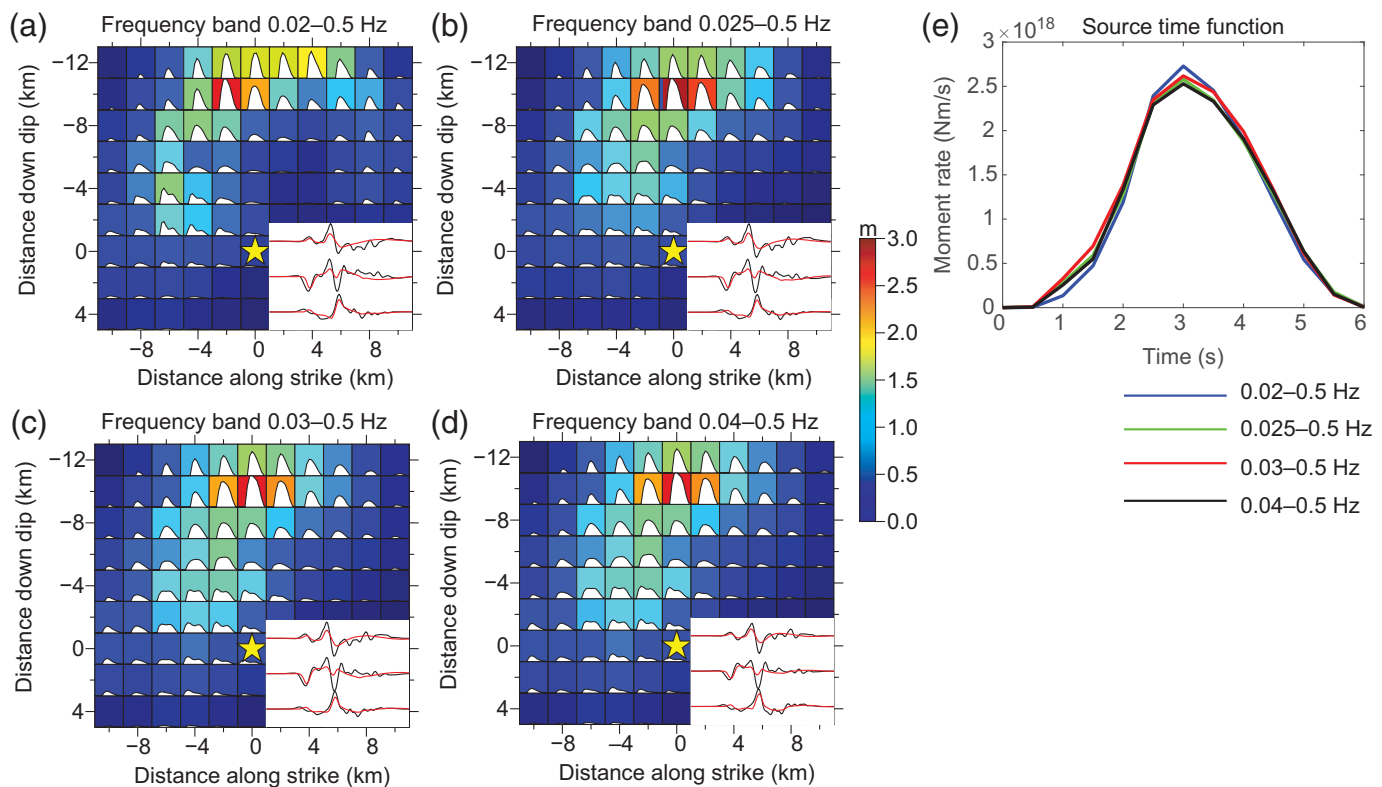
Figure 10. Comparison of the MEMS and strong-motion rupture models. (a,b) The MEMs and strong-motion slip models of the 2021 Yangbi earthquake. (c) Comparison between the STFs of the Yangbi earthquake obtained from the MEMS and strong-motion inversions. (d–f) The same as panels (a)–(c) but for the 2022 Menyuan earthquake. (g–i) The same as panels (a)–(c) but for the 2022 Luding earthquake.

in the original waveforms decrease. For instance, the waveforms at station A0020 mostly have their low-frequency tails removed in 0.04–0.5 Hz. This finding is consistent with the waveform comparisons (Fig. 3 and Figs. S1 and S2) in which the MEMS data are amplified below 0.04 Hz. Therefore, we conclude that raising the lower frequency bound can effectively suppress the low-frequency noises within a certain frequency range, whereas the resulting slip distribution remains stable. Though this could lead to loss of some low-frequency signals, it is still sufficient to obtain satisfactory results for earthquakes with $M_w < 7$. However, it may be necessary to include them in inversions for larger earthquakes of which low-frequency signals are more prominent.

Conclusions

In this study, we applied MEMS waveform data to finite-fault inversions of three strong earthquakes: the 2021 M_w 6.1 Yangbi earthquake, the 2022 M_w 6.6 Menyuan earthquake, and the

2022 M_w 6.6 Luding earthquake. By comparing the MEMS models with those of strong-motion inversions, we found that inversions with densely distributed MEMS recordings produce comparable and sometimes even better rupture models. In the future, the MEMS seismometers may be more and more applied to earthquake monitoring and disaster reduction, because they can be densely deployed in a target area with low cost. In particular, a large amount of near-field MEMS waveform data will become available in China with the completion of the IRREEW network. These abundant data can be

Figure 11. Rupture models of the Menyuan earthquake obtained by inverting the MEMS data in different frequency bands. Panels (a), (b), (c), and (d) show the rupture models using the 0.02–0.5, 0.025–0.5, 0.03–0.5, and 0.04–0.5 Hz frequency bands, respectively. The three-component waveform fittings at station A0020 are shown in the bottom-right corners. (e) STFs obtained using these frequency bands. The normalized misfits of all components in the four inversions shown in panels (a), (b), (c), and (d) are 0.44, 0.47, 0.45, and 0.43, respectively.

used for not only rapid intensity reports and early warning but also for fast source inversion and other related research works, which could help to predict earthquake-related disasters such as landslides.

Data and Resources

Declaration of Competing Interests

Acknowledgments

References

Aizawa, T., T. Kimura, T. Matsuoka, T. Takeda, and Y. Asano (2008). Application of MEMS accelerometer to geophysics, *Int. J. Japanese Comm. Rock Mech.* **4,** 33–36, doi: 10.11187/ijjcrm.4.33.

Bao, X., R. Zhang, T. Wang, A. Shama, R. Zhan, J. Lv, R. Wu, Y. Fu, and G. Liu (2022). The source mechanism and fault movement characterization of the 2022 Mw6.7 Menyuan earthquake revealed by the joint inversion with InSAR and teleseismic observations, *Front. Environ. Sci.* **10,** 917042, doi: 10.3389/fenvs.2022.917042.

Bravo-Haro, M., X. Ding, and A. Elghazouli (2021). MEMS-based low-cost and open-source accelerograph for earthquake strong-motion, *Eng. Struct.* **230,** 111675, doi: 10.1016/j.engstruct.2020.111675.

Cochran, E., J. Lawrence, C. Christensen, and A. Chung (2009). A novel strong-motion seismic network for community participation in earthquake monitoring, *IEEE Instrum. Meas. Mag.* **12,** 8–15, doi: 10.1109/MIM.2009.5338255.

Cochran, E., J. Lawrence, C. Christensen, and R. Jakka (2009). The quake-catcher network: Citizen science expanding seismic horizons, *Seismol. Res. Lett.* **80,** 26–30, doi: 10.1029/2008GL036572.

D'Alessandro, A., R. D'Anna, L. Greco, G. Passafiume, S. Scudero, S. Speciale, and G. Vitale (2018). Monitoring earthquake through MEMS sensors (MEMS project) in the town of Acireale (Italy), *5th IEEE Int. Symp. Inert. Sens. Syst. INERT. 2018*, 1–4, doi: 10.1109/ISISS.2018.8358143.

D'Alessandro, A., S. Scudero, and G. Vitale (2019). A review of the capacitive MEMS for seismology, *Sensing* **19,** 3093, doi: 10.3390/s19143093.

Eddy, D. S., and S. Sparks (1998). Application of MEMS technology in automotive sensors and actuators, *Proc. IEEE* **86,** 1747–1755, doi: 10.1109/5.704280.

Ekström, G., M. Nettles, and M. Dziewoński (2012). The Global CMT project 2004–2010: Centroid-moment tensors for 13,017 earthquakes, *Phys. Earth Planet. In.* **200,** 1–9, doi: 10.1016/j.pepi.2012.04.002.

Holland, A. (2003). Earthquake data recorded by the MEMS accelerometer: Field testing in Idaho, *Seismol. Res. Lett.* **74,** 20–26, doi: 10.1785/gssrl.74.1.20.

Horiuchi, S., Y. Horiuchi, S. Yamamoto, H. Nakamura, C. Wu, P. Rydelek, and M. Kachi (2009), Home seismometer for earthquake early warning, *Geophys. Res. Lett.* **36,** L00B04, doi: 10.1029/2008GL036572.

Kanamori, H., and L. Rivera (2008). Source inversion of W phase: Speeding up seismic tsunami warning, *Geophy. J. Int.* **175,** 222–238, doi: 10.1111/j.1365-246X.2008.03887.x.

Kanamori, H., E. Hauksson, and T. Heaton (1997). Real-time seismology and earthquake hazard mitigation, *Nature* **390,** 461–464, doi: 10.1038/37280.

Kuang, W., C. Yuan, and J. Zhang (2021). Real-time determination of earthquake focal mechanism via deep learning, *Nat. Commun.* **12,** 1432, doi: 10.1038/s41467-021-21670-x.

Laske, G., G. Masters, Z. Ma, and M. Pasyanos (2012). CRUST1.0: An updated global model of Earth's crust, *Geophys. Res. Abs.* 14, 3743.

Lawrence, J., E. Cochran, A. Chung, A. Kaiser, C. Christensen, R. Allen, J. Baker, T. Heaton, D. Kilb, M. Kohler, and M. Taufer (2014). Rapid earthquake characterization using MEMS accelerometers and volunteer hosts following the M 7.2 Darfield, New Zealand, earthquake, *Bull. Seismol. Soc. Am.* **104,** 184–192, doi: 10.1785/0120120196.

Li, J., M. Böse, Y. Feng, and C. Yang (2021). Real-time characterization of finite rupture and its implication for earthquake early warning: Application of FinDer to existing and planned stations in southwest China, *New Front. Earthq. Early Warning Sys.* **9,** 111–130, doi: 10.3929/ethz-b-000499514.

Li, W., Y. Huang, X. Wang, X. Jiang, X. Li, X. Xie, Q. Wang, and H. Yan (2022). Source model and seismogenic environment of the Ms 6.4 Yangbi earthquake in Yunnan, China—based on InSAR observation, *Appl. Sci.* **12,** 5908, doi: 10.3390/app12125908.

Li, Y., W. Jiang, Y. Li, W. Shen, Z. He, B. Li, Q. Li, Q. Jiao, and Y. Tian (2022). Coseismic rupture model and tectonic implications of the January 7 2022, Menyuan Mw 6.6 earthquake constraints from InSAR observations and field investigation, *Remote Sens.* **14,** 2111, doi: 10.3390/rs14092111.

Lin, S. (2011). Research on specification system of seismometers and design of MEMS accelerograph, Institute of Engineering Mechanics, China Earthquake Administration, 4–26.

Lu, H., G. Feng, L. He, J. Liu, H. Gao, Y. Wang, X. Wu, Y. Wang, Q. An, and Y. Zhao (2022). An improved source model of the 2021 Mw 6.1 Yangbi earthquake (southwest China) based on InSAR and BOI datasets, *Remote Sens.* **14,** 4804, doi: 10.3390/rs14194804.

Peng, C., P. Jiang, Q. Chen, Q. Ma, and J. Yang (2019). Performance evaluation of a dense MEMS-based seismic sensor array deployed in the Sichuan-Yunnan border region for earthquake early warning, *Micromachines* (Basel) **10,** 735, doi: 10.3390/mi10110735.

Peng, C., P. Jiang, Q. Ma, J. Su, Y. Cai, and Y. Zheng (2022). Chinese nationwide earthquake early warning system and its performance in the 2022 Lushan M 6.1 earthquake, *Remote Sens.* **14,** 4269, doi: 10.3390/rs14174269.

Peng, C., Y. Zheng, Z. Xu, X. Jiang, and J. Yang (2021) Construction and verification of onsite ground motion prediction models for seismic intensity instrument, *Acta Seismol. Sin.* **43,** 643–655, doi: 10.11939/jass.20210075.

Pozzi, M., D. Zonta, D. Trapani, N. Athanasopoulos, A. Amditis, M. Bimpas, A. Garatsos, Y. Stratakos, and D. Ulieru (2011). MEMS-based sensors for post-earthquake damage assessment, *J. Phys. Conf. Ser.* **305,** 012100, doi: 10.1088/1742-6596/305/1/012100.

Saunders, J., D. Goldberg, J. Haase, Y. Bock, D. Offield, D. Melgar, J. Restropo, R. Fleischman, A. Nema, J. Geng, C. Walls, D. Mann, and G. Mattioli (2016). Seismogeodesy using GPS and low-cost MEMS accelerometers: Perspectives for earthquake early warning and rapid response, *Bull. Seismol. Soc. Am.* **106,** 2469–2489, doi: 10.1785/0120160062.

Wang, R., S. Heimann, Y. Zhang, H. Wang, and T. Dahm (2017). Complete synthetic seismograms based on a spherical self-gravitating Earth model with an atmosphere-ocean-mantle-core structure, *Geophys. J. Int.* **210,** 1739–1764, doi: 10.1093/gji/ggx259.

Wells, D., and K. Coppersmith (1994). New empirical relationships among magnitude, rupture length, rupture width, rupture area, and surface displacement, *Bull. Seismol. Soc. Am.* **84,** 974–1002.

Wu, Y. (2015). Progress on development of an earthquake early warning system using low-cost sensors, *Pure Appl. Geophys.* **172,** 2343–2351, doi: 10.1007/s00024-014-0933-5.

Wu, Y., D. Chen, T. Lin, C. Hsieh, T. Chin, W. Chang, W. Li, and S. Ker (2013). A high-density seismic network for earthquake early warning in Taiwan based on low cost sensors, *Seismol. Res. Lett.* **84,** 1048–1054, doi: 10.1785/0220130085.

Yang, H., D. Wang, R. Guo, M. Xie, Y. Zang, Y. Wang, Q. Yao, C. Cheng, Y. An, and Y. Zhang (2022) Rapid report of the 8 January 2022 M_S 6.9 Menyuan earthquake, Qinghai, China, *Earthq. Res. Adv.* **2,** 2772–4670, doi: 10.1016/j.eqrea.2022.100113.

Yang, T., B. Li, L. Fang, Y. Su, Y. Zhong, J. Yang, M. Qin, and Y. Xu (2021). Relocation of the foreshocks and aftershocks of the 2021 Ms6.4 Yangbi earthquake sequence, Yunnan, China, *J. Earth Sci.* doi: 10.1007/s12583-021-1527-7.

Yokota, Y., K. Koketsu, Y. Fujii, K. Satake, S. Sakai, M. Shinohara, and T. Kanazawa (2011). Joint inversion of strong motion, teleseismic, geodetic, and tsunami datasets for the rupture process of the 2011 Tohoku earthquake, *Geophy. Res. Lett.* **38,** 7, doi: 10.1029/2011GL050098.

Yue, H., and T. Lay (2011). Source rupture models for the Mw 9.0 2011 Tohoku earthquake from joint inversions of high-rate geodetic and seismic data, *Bull. Seismol. Soc. Am.* **103,** 1242–1255, doi: 10.1785/0120120119.

Yue, H., Y. Zhang, Z. Ge, T. Wang, and L. Zhao (2020). Resolving rupture processes of great earthquakes: Reviews and perspective from fast response to joint inversion, *Sci. China Earth Sci.* **63,** 492–511, doi: 10.1007/s11430-019-9549-1.

Zhang, B., G. Xu, Z. Lu, Y. He, M. Peng, and X. Feng (2021). Coseismic deformation mechanisms of the 2021 M_S 6.4 Yangbi earthquake, Yunnan Province, using InSAR observations, *Remote Sens.* **13,** 3961, doi: 10.3390/rs13193961.

Zhang, Y., Y. Chen, and L. Xu (2012). Fast and robust inversion of earthquake source Rupture process and its application to earthquake emergency response, *Earthq. Sci.* **25,** 121–128, doi: 10.1007/s11589-012-0838-2.

Zhang, Y., R. Wang, J. Zschau, Y. Chen, S. Parolai, and T. Dahm (2014). Automatic imaging of earthquake rupture processes by iterative deconvolution and stacking of high-rate GPS and strong motion seismograms, *J. Geophys. Res.* **119,** 5633–5650, doi:10.1002/2013JB010469.

Zheng, X., Y. Zhang, and Q. Ma (2018) Fast inversion of rupture process based on strong motion data and the feasibility of its automation, *Chin. J. Geophys.* **61,** 4021–4036 (in Chinese).

Zheng, X., Y. Zhang, and R. Wang (2017) Estimating the rupture process of the 8 August 2017 Jiuzhaigou earthquake by inverting strong-motion data with IDS method, *Chin. J. Geophys.* **60,** 4421–4430 (in Chinese).

Zheng, X., Y. Zhang, R. Wang, L. Zhao, W. Li, and Q. Huang (2020). Automatic inversions of strong-motion records for finite-fault models of significant earthquakes in and around Japan, *J. Geophys. Res.* **125,** e2020JB019992, doi: 10.1029/2020JB019992.